Astronomically forced climate change in the late Cambrian

Aske L. Sørensen[1], Arne T. Nielsen[2], Nicolas Thibault[2], Zhengfu Zhao[2], Niels H. Schovsbo[3], Tais W. Dahl[1*.]

[1] GLOBE Institute, University of Copenhagen, Denmark.

[2] Department of Geosciences and Natural Resource Management, University of Copenhagen, Denmark.

[3] Geological Survey of Denmark and Greenland (GEUS), Denmark.

*Corresponding author: tais.dahl@sund.ku.dk, ORCID ID: 0000-0003-4629-8036

Abstract

We report evidence for Milankovitch cycles in two drill cores from the Cambro–Ordovician Alum Shale Formation of Scandinavia. The signal is preserved in elemental abundances recorded at high stratigraphic resolution by core scanning XRF analysis (0.2 mm resolution). The new data enable us to establish a floating timeline calibrated to the stable 405 kyr eccentricity cycle for a ~8.7 Myr interval across the Miaolingian–Furongian boundary. This interval spans the Steptoean Positive Carbon Isotope Excursion (SPICE), which is recorded in the $\delta^{13}C_{org}$ in the studied drill cores. We calculate the durations of the *Olenus* Superzone to 3.4 ± 0.2 Myr, the *Parabolina* Superzone to 1.9 ± 0.3 Myr, the *Leptoplastus* Superzone to 0.33 ± 0.18 Myr, the *Protopeltura* Superzone to 0.51 ± 0.20 Myr, and the SPICE event straddling the Paibian and lower main part of the Jiangshanian Stage to 3.0 ± 0.2 Myr. The sedimentation rate shows similar trends at both drilling locations and is inversely correlated to eustatic sea level changes in certain time intervals, opening tantalizing new prospects of using cyclostratigraphic analyses of shales to track eustatic sea level variations. The identification of obliquity cycles enables us to calculate the Cambrian Earth–Moon distance as well as the day length at ~493 Ma to $368.9 \pm 2.3 \cdot 10^6$ m and 21.78 ± 0.29 hours, respectively.

Keywords: Cyclostratigraphy, Core Scanning XRF, Alum Shale, SPICE event, Earth–Moon distance, Furongian

1. Introduction

The Cambrian was characterized by a warm "greenhouse" climate with seawater temperatures exceeding 30°C in the tropics, 20–25°C at ~65–70°S, and ~15°C at the poles with no sea ice or continental ice sheets on the South Polar continent (Hearing et al., 2018; Wotte et al., 2019). Nevertheless, evidence of rapid and dramatic sea level changes have been interpreted in the context of glacio-eustasy, since ice-albedo feedbacks are known to be powerful amplifiers of astronomical insolation forcing (Babcock et al., 2015). A long-term sea level rise of at least 200 m occurred through the Cambrian while Laurentia, Baltica, Siberia and Avalonia separated and drifted away from Gondwana (Peng et al., 2012). Baltica – in focus in the present study – was located at mid southerly latitudes (Fig. 1A).

The Cambrian marks an important phase in the history of life on Earth, with rapid evolution of the marine animal ecosystems. The period was also characterized by several major changes in the Earth's carbon cycle that are expressed in carbon isotope excursion events (Bambach et al., 2004; Peng et al., 2012). One of these events is the Steptoean Positive Carbon Isotope Excursion (SPICE) recorded in the early Furongian (late Cambrian) by a large positive shift in the $^{13}C/^{12}C$ ratio in marine sedimentary successions worldwide (Saltzman et al., 2000). The SPICE event was associated with a large disturbance in the global marine cycles of sulfur, molybdenum and uranium, suggesting an extensive expansion of marine anoxia in the oceans (Gill et al., 2011; Dahl et al., 2014).

The Cambrian timeframe is constrained by only a few radiometric ages that can be more or less reliably correlated to cosmopolitan stage boundaries (Ogg et al., 2016). The Miaolingian (Cambrian global stages 5–7, ~509 – 497 Ma) and Furongian (Cambrian stages 8–10, ~497–485.4±1.9 Ma) together straddle approximately 24 Myr and 20–30 agnostid trilobite biozones (not all global) (Peng et al., 2012; Ogg et al., 2016). The average durations of the individual stages can be calculated by linear interpolation, assuming each biozone represents an equal length of time (Peng et al., 2012). However, this assumption is almost certainly wrong. Thus, a fundamental motivation for this study is to improve the temporal framework for the late Cambrian and across the SPICE event. This will pave the way for a better understanding of the trigger and dynamic feedbacks at play during this biogeochemical event.

The identification of astronomically forced climate cycles expressed in sedimentary successions can be used to refine the temporal resolution of the geological time scale. Once Milankovitch cycles are recognized in the stratigraphic record, they can be used to establish a relative ‘floating’ timescale. This approach has long been applied to Cenozoic and Mesozoic sediments (Hinnov, 2018 and references therein), but recent studies have pushed the method further back into the Paleozoic, e.g. Permian (Wu et al., 2013; Fang et al., 2017), Carboniferous (Davydov et al., 2010), Devonian (De Vleeschouwer et al., 2012; De Vleeschouwer et al., 2015; Ellwood et al., 2015; Da Silva et al., 2016; Pas et al., 2018), Silurian (Gambacorta et al., 2018), Ordovician (Fang et al., 2016), and even into the Proterozoic (e.g. Zhang et al., 2015) and Neoarchean (Walker and Zahnle 1986; Hofmann et al., 2004; de Oliveira Carvalho Rodrigues et al., 2019). So far, applications to the Cambrian are limited to only one section covering a ~1.4 Myr interval across the Drumian–Guzhangian boundary in China (Fang et al., 2020), although thick cyclic sequences of shallow marine carbonate platforms are found globally (Derby et al., 2012) and have already been suggested to record astronomically forced sea level oscillations (Osleger & Read, 1991).

Cyclostratigraphic tuning relies on accurate astronomical modeling of the planetary orbital motions which becomes challenging prior ~50 Ma (Laskar et al., 2004). The chaotic nature of the Solar System makes it impossible to predict the exact phases and amplitudes of the 100-kyr and 405-kyr eccentricity components beyond ~50 and ~200 Ma, respectively. Nonetheless, modeling and observations suggests that the 405 kyr eccentricity period has been stable throughout Earth's history, making it the prime calibration target for pre-Cenozoic sequences (Laskar et al., 2004). Calibrations combining cyclo- and chronostratigraphy confirm this is the case, and the 405 kyr eccentricity period is found to be stable to within ~10% uncertainty as far back as ~1.4 Ga (Zhang et al., 2015). In contrast, the obliquity and precession periods have changed due to the dissipative effects of the Earth–Moon system that result in lunar recession, longer day length, slower obliquity and precession rates of the Earth. Thus, empirical constraints on these Milankovitch periods from the geological record illuminate the exchange of angular momentum and energy within the Earth–Moon system and the orbital evolution of the Solar System.

Here we report evidence for Milankovitch cycles across a ~8.7 Myr long time interval in the late Cambrian. We are using high resolution (0.2 mm) XRF core scanning to investigate cyclic patterns in the elemental abundances of an organic-rich, slowly deposited black shale (Alum Shale) in two drill cores from southern Scandinavia. Identification of the stable 405 kyr eccentricity cycle is used to construct a floating astronomical time scale and constrain the duration of late Cambrian biozones and the SPICE event. The new data also constrains the Earth's precession and obliquity periods and resolve the day length and Earth–Moon distance at ~493 Ma. Furthermore, our cyclostratigraphic calibration allows us to reconstruct sedimentation rates that we compare to changes in eustatic sea level, inferred from sequence stratigraphy.

2 Materials and Methods

2.1 Geological setting

The Alum Shale Formation predominantly consists of laminated, organic-rich mudstone with high pyrite content. A few thin primary limestone beds occur in the middle Cambrian part (Nielsen and

Schovsbo, 2007), but bituminous limestone concretions and beds (so-called anthraconite or orsten) are common throughout the unit and constitute up to 50% of the stratigraphic thickness in south central Sweden. Limestone concretions account for 5–10% of the stratigraphic thickness in Scania-Bornholm, the area in focus in the present study (southernmost Sweden and Denmark). The Alum Shale Formation, which is up to ~100 m thick in Scania and ~40 m on Bornholm, was deposited from the Miaolingian through earliest Ordovician (Tremadocian) in the deeper parts of an epicontinental sea covering the (current) western part of Baltica. At this time, Baltica was presumably located at ~30–60°S (Fig. 1A) and the Alum Shale was deposited from about the storm wave base and deeper (Buchardt et al., 1997; Nielsen & Schovsbo, 2015). Sedimentary supply was extremely low, reflecting that the craton was intensively peneplained, and compacted accumulation rates for the Alum Shale averages 1-2 mm/kyr with maximum of 5 mm/kyr in the Southern part of Scandinavia (Nielsen et al., 2018). Reworking caused by lowering of the storm wave base during sea level lowstands occurred repeatedly in the paleo-inboard part of the Alum Shale basin (south central Sweden), but generally are not seen in Scania-Bornholm, representing the deepest part of the basin (Nielsen & Schovsbo, 2015). Deposition took place under predominantly euxinic conditions and the shale is renowned for its high content of syngenetically enriched redox sensitive elements, including Mo, U, and V (Dahl et al., 2019, and references therein). Nonetheless, bottom-water oxygenation occurred episodically and the shale is rich in fossils, notably trilobites. Nine superzones, subdivided into 31 biozones, are defined for the Miaolingian–Furongian interval in Scandinavia, providing a high-resolution stratigraphic framework for study of the Alum Shale (Fig. 1D) (for review, see Weidner & Nielsen, 2014; Nielsen et al., 2020).

Figure 1 here

The present study focuses on the Miaolingian–Furongian boundary interval in two drill cores from southern Scandinavia, namely Fågeltofta-2 (Få-2), and Billegrav-2 (Bi-2) (Fig. 1). The studied interval spans the *A. pisiformis* Zone (Miaolingian) and the *Olenus* and *Parabolina* Superzones (Furongian) in both cores, and continues further up into the *Leptoplastus*, *Protopeltura* and *Peltura* Superzones in the Bi-2 core. For remarks on the informal terms 'lower' and 'upper' *Olenus* Superzone, see Nielsen et al. (2020). The cores have been kept as intact as possible and no further splitting has been undertaken in the search for fossils. Correlation is facilitated both by identification of characteristic fossils, incidentally exposed on the surfaces of broken core pieces, and the gamma ray logs recorded in the drill-holes. The stratigraphic framework for Bi-2 are described in Nielsen et al (2018), and we list first and last fossil appearances for Få-2 along with the selected boundaries based on GR log data comparison to three other cores (see details in Table S4).

The Få-2 and Bi-2 wells were drilled in 1997 and 2010, respectively. Since then, the cores have been stored at the Natural History Museum of Denmark (Få-2) and the Geological Survey of Greenland and Denmark (Bi-2). Both cores had a patchy white coating on their surfaces (presumably a sulfate mineral resulting from incipient break down of pyrite), which was thoroughly washed off using demineralized water prior to XRF analysis.

2.2 Core scanning

The elemental composition of the cores was analyzed using an Itrax X-Ray Fluorescence (XRF) core scanner from Cox Laboratories at the GLOBE Institute, University of Copenhagen. The core recovery is close to 100% and overall, the cores are intact so that successive core pieces easily can be fitted together. The core pieces were assembled using a Cl-rich dough, allowing gaps to be easily identified by XRF and removed from the analyzed signal (see details in the supplementary information, SI). The core scanner is equipped with a rhodium tube as the X-Ray source. Scanning was done at a vertical resolution of 0.2 mm for 7 seconds per analysis with a voltage and current on the Rh-tube of 30 kV and 50 mA, respectively. Scanning was performed on the outer, round surface of the drill cores (diameter of 55 mm) that exceeds the width of the scanned area of 10 mm. The XRF signal was recorded with the "CoreScanner 8.6.4 Rh" software and the XRF signal was converted to elemental concentrations using Q-spec with USGS SGR-1 (Green River Shale) as reference material. A total of 26 and 28 different elements were measured in Få-2 and Bi-2, respectively. A detailed description of quality control measures is provided in the SI.

2.2.1 Data processing

As a first step, we removed high frequency noise and detrended the signal of the element of interest. To remove high frequency (>0.5 mm^{-1}) noise from the elemental signal, the elemental data were first smoothed using the "loess" function in Matlab with a window of 25 points corresponding to ~5 mm weighed smoothing (i.e. likely ~2 kyr on average). This procedure reduces noise from the analyzed signal with only minimal risk of overlooking Milankovitch cycles that operate over longer time scales. This translates into a longer exposure time (175 s) sufficient for detection of Mo and major elements relevant in this study (see details in the SI). Diagenetic limestone intervals were identified both visually and chemically and omitted from the cyclostratigraphic analysis based on the assumption that they represent very short time (see discussion in section S1.5). In total, these intervals accounts for 8.0% (1.7 m) and 1.4 % (0.23 m) of the studied stratigraphy in Få-2 and Bi-2 core, respectively (see Fig. S3). This step has only minor effects on our results, as discussed in section 4.2. As remarked above, broken core pieces were assembled using a Cl-rich dough, allowing gaps to be easily identified and removed from the data set (see SI for details). Long-term trends were removed from the elemental data (detrended); for example: a third and a tenth-degree polynomial were fitted to the sulfur data to produce detrended S signals for Få-2 and Bi-2, respectively (see Fig. S3 for details).

2.2.2. Time series analysis

The detection of Milankovitch cycles was performed in a series of steps. First, stratigraphic cyclic variations in the sulfur data and other elements were studied using both wavelet and the multi-taper method (MTM) spectral analysis (Thomson, 1982). We performed the MTM spectral analysis using Matlab's 'pmtm' function, where number of tapers = 2·nw-1, nw = time-halfbandwidth = 2.5, and nfft = number of points in the discrete Fourier transform = number of data points in the discrete data series. For the wavelet analysis we used continuous 1D wavelet transform (the 'cwt' function in Matlab) with the 'bump' wavelet. The significance of the periods identified in the MTM analyses was determined against "the bending power law" (BPL) and the "Auto Regressive Moving Average" (ARMA) as noise model (Vaughan et al., 2011). These noise models have been considered as more robust than the typical autoregressive AR(1) model often favored in cyclostratigraphic studies (Vaughan et al., 2011) (Fig. S4). Confidence levels (CL) for the MTM were calculated using the method of Mann & Lees (1996). The identified cycles were isolated using Taner band-pass filtering (Taner et al., 1979). In this way, the "filtered output" shows the Milankovitch-forcing of each of the dominant modes.

To verify that the dominant periods in the observed signal could be forced by Milankovitch-driven solar insolation, we compared the frequency ratios of the dominant modes to the theoretically predicted ratios for the late Cambrian according to Milankovitch theory (Waltham 2015).

The floating age model and sedimentation rates were obtained by identifying maxima of the 405 kyr eccentricity cycle (E_{405}). The final age model was constrained by simultaneous correlation of biozones, stratigraphic Mo curves, and counting E_{405} cycles in the filtered outputs in the two cores. The Mo curves correlate well with the gamma-log pattern, but provide a much higher stratigraphic resolution. All data presented in the time domain were calibrated to a smoothed version of 405 kyr derived sedimentation rates using a polynomial fit (Fig. 6A). This is done to prevent abrupt shifts in the sedimentation rate across the anchored 405 kyr eccentricity maxima (Fig. 6A, black curves). Further, we used the automated eCOCO algorithm to confirm that our sedimentation rate curves are correct (Fig. 6A, grey circles; Li et al., 2019). The obtained floating astronomical time scale was anchored at the ~497 Myr date for the Miaolingian/Furongian boundary (Peng et al., 2012). Cyclic amplitude modulations in precession cycles were tested using Taner band-pass filtering and Hilbert transformation (Taner et al., 1979).

2.3 Carbon isotopes

The carbon isotope composition and total organic carbon content were measured in 48 and 79 Alum Shale samples taken from the Bi-2 and Få-2 cores, respectively. Samples of ~1–3 g were collected from the cores and powdered in an agate mortar. Homogenized portions of powder (~20 mg) were loaded into tin capsules, then acid fumigated with 12 M HCl and dried to remove inorganic carbon and remaining water. Subsequently, the total organic carbon content and the $^{13}C/^{12}C$ ratios were analyzed at the University of Copenhagen using an elemental analyser (CE1110, Thermo Fisher Electron, Milan, Italy) coupled in continuous flow mode to a Finnigan MAT Delta PLUS isotope ratio mass spectrometer (Thermo Fisher Scientific, Bremen, Germany). For calibration, we used a pure CO_2 gas calibrated against a certified ^{13}C-sucrose (IAEA, Vienna, Austria). For quality control, we used certified reference materials of loamy soil (calibrated by Elemental Microanalysis, Okehampton, UK). The reproducibility of reference material analyses was ±0.08‰ (SD).

3 Results

3.1 Identification of elemental cycles

The Alum Shale lithology is very monotonous and exhibits no visible signs of cyclicity (Fig. 1C), and appears, at first glance, a poor choice for cyclostratigraphic analyses. However, the slow undisturbed deposition results in an excellent cyclostratigraphic record. The elemental XRF data show pronounced cyclic patterns in the sulfur content in both cores (Fig. 2). Other elements, including clay-bound elements (Si, Al, Ti, K), carbonate (Ca, Mn) and redox sensitive elements (Mo, U, V), also exhibit cyclic patterns, although not as well-defined as the sulfur. Therefore, we focus our cyclostratigraphic analysis on the detrended S signal.

Figure 2 here

3.1.1 Fågeltofta-2 (Scania, Sweden)

Several distinct cycles are recognizable in the MTM spectrum of the detrended S signal from the Få-2 core (Fig. 2A), including ~1.6 m ($p < 0.01$), ~0.44 m ($p \sim 0.06$) and some shorter cycles with a thickness of around ~0.13 m ($p < 0.01$). The ratios between these frequencies fit with the predicted Milankovitch periods for the Cambrian (Waltham, 2015). If we ascribe the ~1.6 m cycle to the 405 kyr eccentricity cycle, then the ~0.44 m and ~0.13 m cycles would roughly correspond to ~100 kyr short eccentricity and ~32 kyr obliquity cycles, respectively. Below, we further verify this choice with independent data from Bi-2 and an age model that fits all available chemo, chrono- and biostratigraphic data. Furthermore, we confirmed this interpretation using the Bayesian inverse method called 'TimeOpt' (see Fig. S8 for details, Meyers 2015).

The 405 kyr (~1.6 m) eccentricity cycle is expressed throughout most of the Få-2 core, but disappears in the upper *Olenus* Superzone between ~74 to 78 m (Fig. 2C). Likewise, the ~100 kyr (~0.44 m) eccentricity cycle is expressed through most of this core, but is absent in the lower *Olenus* Superzone. In the *Parabolina* Superzone at ~69 to 71 m, the ~100 kyr eccentricity cycles appear as two cycles with periods of ~0.5 and 0.35 m, which could correspond to ~95 and 123 kyr, consistent with the ~100 kyr eccentricity cycles (Waltham, 2015). The wavelet spectrogram (Fig. 2D) shows that the ~32 kyr (~0.13 m) obliquity cycle is present with high amplitude in most of the Få-2 core whereas the 18 kyr (~0.07 m) precession cycle is distinguishable only in the lower *Olenus* Superzone, where the precession period varies stratigraphically in parallel with the obliquity cycle. This parallel behavior is reflecting a variable sedimentation rate and is the reason why the precession and obliquity cycle cannot be distinguished from each other in the MTM spectrum (Fig. 2A). Thus, a refined time scale with more precise estimates of the Milankovitch periods can be obtained by taking the variable sedimentation rates into account (see section 3.3. for analyses in time domain).

3.1.2. Billegrav-2 (Bornholm, Denmark)

One significant mode with a period of ~0.7 m ($p < 0.05$) is dominant in the MTM spectrum of the detrended S signal from the Bi-2 core (Fig. 2B). The wavelet analysis (Fig. 2D) reveals that higher frequency cycles are also expressed with periods of ~0.23 m and ~0.06 m (Fig. 2D). The ~0.17 m period is present in the *A. pisiformis* Zone, the upper *Olenus* and the *Peltura* Superzones, and the ~0.06 m period cycles are recognizable in shorter intervals from the mid *Olenus* Superzone to the end of the *Peltura* Superzone. Figure 2D also shows that the ~0.7 m cycle is expressed from the lower *Olenus* Superzone to the top of the studied interval (~103–114 m), but is absent in the *A. pisiformis* Zone.

If the 0.7 m cycle corresponds to the 405 kyr eccentricity cycle, then the ~0.17 m and ~0.06 m may correspond to the ~100 kyr eccentricity and the 32 kyr obliquity cycles consistent with the expected Milankovitch periods for the Cambrian (Waltham, 2015).

3.2 Age model

A floating astronomical time scale for the late Cambrian was established by calibration the signal to the stable 405 kyr eccentricity cycles (Fig. 3). In total, we identify thirteen 405 kyr eccentricity cycles in Få-2 and twenty-one complete cycles in Bi-2. Correlation is constrained by trilobite and gamma log stratigraphy, as well as Mo trends, and there is a good match between the two cores regarding the eight cycles identified in the *Olenus* Superzone (Fig. 3). Five well-expressed E_{405} cycles are recognized in the *Parabolina* Superzone of the Få-2 core and four in the Bi-2 core, where a cycle thus seems to be missing. Cycles Pa-4 and Pa-5 can be recognized in both cores, which leaves Pa-1, Pa-2 or Pa-3 as candidates for the missing cycle on Bornholm. The E_{405} filtered output for these cycles also looks perturbed in Bi-2 (Fig. 3) and we interpret this as a hiatus approximately spanning the duration of Pa-2. This hiatus happens to coincide with the presence of brachiopod coquinas in the *Parabolina* Superzone on Bornholm (see e.g. Hansen, 1945), which could indicate winnowing of Alum Shale mud associated with sea level lowstand conditions (cf. Nielsen & Schovsbo, 2015). Apart from this hiatus and the Ol-7 cycle in the Bi-2 core, all E_{405} cycles appear well-expressed in both cores allowing for cycle counting. No obvious perturbations can be observed in the two wavelet transforms suggesting absence of other significant hiatuses and/or condensed intervals and it further supports our methodology with removal of anthraconite concretions prior to analysis (Fig. 2, S3).

Because the very top of the Furongian is not included in the studied interval, we cannot number our 405 kyr cycles downwards across all stages as recommended by Hilgen et al. (2020) and instead we employ a downward numbering of cycles for each superzone (Fig. 3).

Figure 3 here, 1 page width (18x14cm)

3.3 Analyses in time domain and amplitude modulations

The duration of the dominant orbital periods can be derived more precisely by analyzing the spectrum of the series calibrated to the 405-kyr eccentricity rhythm (Fig. 4). This analysis also allows us to investigate potential amplitude modulations of the dominant periods (Fig. 5), which helps to validate the astronomical interpretation of the observed stratigraphic cycles.

In addition to the 405 kyr eccentricity cycles, the Få-2 MTM power spectrum of the entire studied interval (Fig. 4A) shows spectral peaks at ~32 kyr ($p < 0.01$) and ~124 kyr ($p < 0.1$). In the lower part of the *Olenus* Superzone of Få-2, two peaks of ~18 kyr ($p < 0.05$) and a ~32 kyr ($p < 0.01$) is also clearly expressed (Fig. 4C). These modes are consistent with the estimated periods of the Cambrian precession (~18 kyr) and obliquity (~32 kyr), while the 124 kyr peak is close to one of the two expected main frequencies (93 and 130 kyr) of the short-eccentricity band (Waltham, 2015).

In Bi-2, the MTM power spectrum of the entire studied interval (Fig. 4B) shows three spectral peaks within the short-eccentricity band at 114 kyr ($p < 0.05$), 88 kyr ($p < 0.05$) and 80 kyr ($p < 0.01$). An MTM spectrum focused on the upper *Olenus* Superzone interval highlights a spectral peak of the obliquity cycle at ~30 kyr ($p < 0.01$) along with two spectral peaks at ~93 and ~130 kyr (Fig. 4D). These modes are also consistent with the published estimates of the Cambrian obliquity (~30 kyr) and ~100 kyr eccentricity (93 and 130 kyr) periods (Waltham, 2015).

Visualizations of specific intervals, including the *Protopeltura* and *Leptoplastus* Superzones, are included in the SI.

Figure 4 here (1/2 page width (one column) (9x22cm))

The 18 kyr precession component expressed in the lowermost *Olenus* Superzone of the Få-2 core (Fig. 4D) exhibits amplitude modulations with a characteristic period consistent with the ~100 kyr eccentricity period. We calculate an average duration of 103 kyr from six cycles in the precession envelope (Fig. 5).

We also observe a marked shift in the dominant mode of oscillations in the detrended sulfur signal across the Miaolingian–Furongian boundary in the Få-2 core changing from ~32 kyr cycles (obliquity) to ~18 kyr cycles (precession) (Fig. 5). This orbital shift from obliquity-dominated to precession-dominated sedimentation coincides with onset of the SPICE event (Fig. 6). This shift in cyclicity could not be verified in the Bi-2 core where high-frequency cycles have not been identified in this interval.

Figure 5 here (1 page width, 18x6cm)

3.4 Carbon isotope stratigraphy

Both cores exhibit a +1.5‰ positive $\delta^{13}C_{org}$ excursion from the *A. pisiformis* Zone into the *Olenus* Superzone known as the SPICE event (Fig. 6E). The Bi-2 curve is similar in magnitude and absolute values to that found in the Andrarum-3 drill core, Scania, Sweden (Ahlberg et al., 2008; Balslev-Clausen et al., 2013) obtained some 7 km NW of Fågeltofta. The $\delta^{13}C_{org}$ values of Få-2 are ~1 ‰ lower than that of Bi-2, but the SPICE excursion displays the same magnitude and timing at both drill sites (Fig. 6E). The onset of the SPICE event is difficult to determine since $\delta^{13}C_{org}$ steadily increases from the base of the Drumian (Ahlberg et al. 2008). Here, we consider the end of the SPICE event as the level where the $\delta^{13}C_{org}$ curve return to steady values, and define the onset of SPICE where the $\delta^{13}C_{org}$ curve intercepts that post-excursion level.

4. Discussion

The sulfur content varies in a cyclic manner with up to four characteristic periods observed across ~5.3 and 8.7 Myr long intervals in the two late Cambrian drill cores. The ratios between these periods are in good agreement with the Milankovitch theory (Waltham, 2015) suggesting that the cyclic sedimentation was driven by variation in solar insolation.

This interpretation is corroborated by numerous observations in our data set, which we discuss below. First, we estimate the duration of biozones and find they are consistent with previous constraints (Section 4.1.1). Secondly, we determine the sedimentation rates in the two cores and show that they also align with previous estimates and vary in parallel as expected if the sedimentary supply was controlled by sea level changes (Section 4.1.3). Thirdly, we calculate the obliquity period and find that it fits with available data and models for the evolution of the Earth–Moon system (Section 4.2). All of these results contribute to verify that these cycles, detected in the Alum Shale Formation, were astronomically forced by variation in solar insolation. We therefore consider the data reported here as a robust identification of astronomically forced climate change in the late Cambrian.

4.1. Implications for the Cambrian time scale and sea level changes

4.1.1. Durations of biozones

According to the age model (Section 3.2), the *Olenus* Superzone (Paibian Stage) spans ~8.2 and 8.5 E_{405} cycles in the Få-2 and Bi-2 cores, respectively (Fig. 3). From this, we estimate the duration of the *Olenus* Superzone to 3.4 ± 0.2 Myr. This figure is similar to, but far better constrained than previous interpolated duration of the Paibian Stage at ~3 Myr (Peng et al., 2012). The *Parabolina* Superzone spans 4.8 E_{405} cycles in the Få-2 (Fig. 3) suggesting a duration of 1.9 ± 0.3 Myr (Fig. 6). This duration relies on the E_{405} cycles in the Få-2 core since a hiatus appears to be present in this interval of the Bi-2 core (section 3.2). Based on the Bi-2 core, we estimate a duration of the *Protopeltura* and *Leptoplastus* Superzones at 0.49 ± 0.22 Myr and 0.32 ± 0.18 Myr, respectively (Fig. 3 and Fig. S7, see SI for details regarding the calculation).

The reported uncertainties are conservative estimates that include uncertainty of the biozone boundaries plus uncertainty of the peak assignments in the cyclostratigraphic signal. Based on the tight biostratigraphic constraints (Nielsen et al., 2018, Table S4), we assume that the biozones boundaries are determined with a maximal offset of 100 kyr in both cores, and that odd peak shapes contribute 100 kyr uncertainty for most superzones and 200 kyr uncertainty for the *Parabolina* Superzone (due to the odd shape of Pa-1 in Bi-2). In total, our biozone durations are estimated to carry ~200-300 kyr uncertainty, in good agreement with the observed discrepancy of the duration of the *Olenus Superzone* (~0.3 E_{405} kyr = ~133 kyr) derived from comparison of the two cores.

4.1.2. Duration of the SPICE event

The onset of this isotope excursion is located at the base of cycle Ap-1 in the upper part of the *Agnostus pisiformis* Zone. A return to the pre-excursion values, here taken to define the upper boundary of the event, is seen in the middle of the Ol-2 cycle in the upper *Olenus* Superzone (Fig. 6). Defined this way, the SPICE event straddles 7.5 ± 0.5 E_{405} cycles, and, accordingly, the duration becomes 3.0 ± 0.2 Myr.

The SPICE event has been previously documented in both carbonate ($\delta^{13}C_{carb}$) and organic carbon ($\delta^{13}C_{org}$) in marine sedimentary sequences worldwide. However, Saltzman et al. (2011) demonstrated that $\delta^{13}C_{org}$ records show an increasing trend that precedes that of $\delta^{13}C_{carb}$ in most investigated sections. Also, we note that anomalously low $\delta^{13}C$ values are found immediately below the SPICE event in the Drumian and Guzhangian part of the Alum Shale Formation (Ahlberg et al. 2008; Balslev-Clausen et al. 2013). To date, our study represents the first attempt to precisely determine the duration of the SPICE excursion. We stress that the calculated duration refers to the $\delta^{13}C_{org}$ excursion in the shales. Further, a clear distinction must be made between the duration of the SPICE event and the duration of the associated oceanic anoxic event (Gill et al., 2011; Dahl et al 2014; see also Nielsen & Schovsbo 2015, fig. 10). The SPICE event records an interval with anomalous high $\delta^{13}C$ values in the oceans, whereas the coinciding global expansion of anoxic water masses appears to straddle a shorter stratigraphic interval (Dahl et al. 2014). It has been suggested that the longer-term drop in Mo concentrations observed at the base of the Furongian represents a global Mo drawdown due to expansion of anoxic water masses at that time (Gill et al. 2011). Our data show that the onset of Mo drawdown coincides with the base of the *Olenus* Superzone as marked by a sudden decrease in Mo, whereas a return of Mo in the middle of Ol-6 marks a significant change in slope from relatively stable to increasing Mo content (Fig. 6). Accordingly, these observations suggest that the interval of intensified Mo drawdown associated with expanded ocean anoxia spans 2.5 ± 0.5 E_{405} cycles corresponding to a total duration of 1.0 ± 0.2 Myr in the earliest Furongian.

4.1.3. Sedimentation rates and sea level changes

The sedimentation rate calculated for the Få-2 core varies from 3.2 – 4.5 mm/kyr, which is about twice of the 1.3 to 2.2 mm/kyr calculated for Bi-2 (Fig. 6A). For both cores, reconstructed sedimentation rates show a small increase across the Miaolingian–Furongian boundary, a steep decline in the lower *Olenus* Superzone followed by an increase upwards through the upper *Olenus* Superzone reaching a maximum near the *Olenus – Parabolina* Superzone boundary. The variable sedimentation rates derived using the eCOCO analysis matches well with this trend for most of the stratigraphy (Fig. 6A). A comparison between sedimentation rate and sea level changes shows intervals of inverse correlation (Fig. 6B). Specifically, the well constrained sea level drop through the upper *Olenus* Superzone is coupled to faster sedimentation at Få-2. Yet, there is no universal correlation between sedimentation rates and inferred sea level.

This observation suggests that both study locations were closer to the sediment source during lower sea level, just as should be expected. The differences in stratigraphic thicknesses between Bornholm and Scania is ascribed to uplift of the Bornholm area, located closer to the edge of the Baltica craton, see Nielsen et al. (2018) for details. In any case, the parallel changes in sedimentation rates within the Alum basin inferred from our cyclostratigraphic analyses, might open new prospects for reconstructing eustatic sea levels in the past.

Figure 6 here

4.2. Obliquity period, Earth–Moon distance and length of the Cambrian day

During geological time, dissipative effects in the Earth–Moon system have caused the Moon to migrate away from the Earth, slowing down Earth's rotation as well as the obliquity and precession periods (Waltham, 2015). Our new constraint on Earth's obliquity period in the early late Cambrian nicely illustrates this process.

The best estimate of the obliquity period is obtained from a continuous interval that preserves many characteristic cycles. The Jiangshanian interval (*Parabolina* Superzone) from 67.25 to 72.5 m in the Få-2 core spans 1.24 Myr (according to the Få-2 sedimentation rate, see Fig. 6) and preserves four well-defined 405 kyr eccentricity cycles (Pa-1, Pa-2, Pa-3 and Pa-4) and 39 well-defined obliquity cycles (Fig. 7).

Figure 7 here (width: one page)

Based on these data, we can calculate an average obliquity period of 31.9 ± 1.2 kyr for the mid-Furongian, where the error represents the uncertainty derived from counting statistics of 39 obliquity cycles. We consider this as an upper estimate for the obliquity period because the removal of limestone intervals (which reduced the total stratigraphic thickness by 7.95 % in this interval) might induce a systematic bias. The limestone nodules contain on average ~20 % clay (Buchardt & Nielsen, 1985), which implies a five-fold greater thickness for the uncompacted limestone in comparison with the equivalent (compacted) shale, as the limestone cement represents a measure for the original porosity. Accounting for this, we find the obliquity period was 31.4 ± 1.2 kyr at ~493 Ma. This period is also consistent with an independent estimate of ~30 kyr obtained from the MTM spectrum of the later Paibian interval (upper *Olenus* Superzone) from 109.4 to 113.0 m in Bi-2 (Fig. 4D). Note that this ~30 kyr spectral peak carries significant uncertainty (Fig. 4D), since it is mainly controlled by high amplitude obliquity cycles in a short stratigraphic interval at ~111.2 – 111.5 m (see Fig. 2D) well within one 405 kyr cycle (~0.7 m in Bi-2). In any case, the new precise estimate of the obliquity period is perfectly consistent with previously reported values for the early Paleozoic, including ~30.7 kyr at ~504 Ma (Fang et al. 2020) and ~30.6 kyr at ~465 Ma (Zhong et al. 2018).

The Cambrian day length, Earth's axial precession, and the Earth–Moon distance can be calculated from the obliquity period due to conservation of angular momentum in the Earth–Moon system (Walker & Zahnle, 1986; Lowrie, 2007; Huang et al., 2020). Using the same equations (see SI), we calculate an axial precession of 21.56 ± 0.57 kyr, an Earth–Moon distance of $368.9 \pm 2.3 \cdot 10^6$ m, and a day length of 21.78 ± 0.29 hours in the late Cambrian (~493 Ma). Here, the uncertainty is the propagated error from the obliquity estimate. These results address a long-standing scientific conundrum of how the Moon has migrated away from the Earth. The lunar recession has been approximately at 'present rate' in the past ~250 Ma (Laskar et al., 2004), but was slower in the Paleozoic and Proterozoic (Fig. 8). The 'ocean model' in Fig. 8 predicts a continuous increase in the tidal dissipation rate with time in good agreement with our Cambrian constraint. Interestingly, the late Cambrian day was only slightly longer than would be the case if the Earth-Moon system was resonance-stabilized by the semi-diurnal atmospheric thermal tide at 20.5±1.0 hr, as has been suggested for most of the Proterozoic (Zahnle & Walker 1987, Bartlett & Stevenson 2016). Waltham (2015) compares a range models and calculates the Earth–Moon-distance and day length at 493 Ma to $371.7 \pm 6.8 \cdot 10^6$ m and 22.23 ± 0.90 hours, respectively. The new data from the Alum shale matches Waltham's model predictions with a slower the lunar recession rate in the Paleozoic and provides to date the most precise empirical constraint on the late Cambrian obliquity period, day length and Earth-Moon distance.

Figure 8 here (size: width ½ page 9x6)

4.3. Drivers and responses to astronomically forced climate change in the late Cambrian

The identification of Milankovitch cycles in the Alum Shale Formation implies that sedimentation processes was affected by changes in solar insolation. Below, we discuss plausible scenarios that could have controlled the sedimentary cyclicity.

The simultaneous analyses of multiple elements provide additional clues regarding how the climatic signal was transferred to the sediments. First of all, the cyclicity is well preserved in the bulk sulfur content of the Alum Shale, which is predominantly hosted in pyrite (FeS_2). There is a tight positive correlation between Fe and S content (Pearson correlation coefficient $R > 0.8$, Fig. S1) consistent with iron speciation data showing that almost all iron is hosted in pyrite (Dahl et al., 2010; Gill et al., 2011). Further, Milankovitch cycles are also recorded in the abundances of clay-bound elements, including aluminium (Al), titanium (Ti), potassium (K) and silicon (Si). Importantly, these oscillations are anti-correlated with the sulfur cycles. For example, the Pearson correlation coefficient between detrended Al and S content is –0.77 in the 85.00–88.62 m interval of the Få-2 core where precession and obliquity cycles are well expressed (Fig. 3C, 5, and S5). We note that the amplitudes of clay and pyrite oscillations are of the same order, so that one cyclic variable could potentially drive cycles in the other via dilution.

The Alum Shale was predominantly deposited under euxinic conditions with shorter intervals of oxic bottom waters (Dahl et al., 2010, 2019; Gill et al., 2011). Under these conditions, reactive iron supply to the basin is the main limiting factor for pyrite formation (Raiswell & Canfield, 2012). Therefore, we infer from the negative pyrite–clay correlation that reactive iron was sourced independently of the clay to the basin. This could be the case either for iron transport via aeolian dust and via the benthic iron shuttle (Raiswell & Canfield, 2012). As a first scenario, we suggest that aeolian dust delivery to the Alum Shale sea was linked to seasonal variations driven by insolation, e.g. the spread of drylands and/or changes in the Earth's wind patterns. This concept has been suggested for the orbitally-forced African Monsoon in the middle Holocene (Kutzbach and Liu, 1997), where low seasonal contrast led to lower summer insolation and sea surface temperature, therefore less evaporation, which combined with changes in the Earth's wind systems caused the Sahara desert to spread and increase dust supply to the Mediterranean and Atlantic Ocean.

Alternative scenarios also exist, for example could eustatic sea level variations also affect the benthic iron shuttle and pyrite deposition the Alum Shale sea. There is a positive long-term (>1 Myr) correlation between pyrite content and eustatic sea level in the coress (e.g. *Olenus* and *Parabolina* Superzones in Fig. S3 and Fig. 6), suggesting orbitally-forced sulfur maxima would coincide with sea level maxima. If so, we predict that higher order sea level fluctuations are actually superimposed on the sea level curve shown in Fig. 6.

As another scenario, enhanced weathering has been linked to eccentricity maxima and greater seasonal contrast (Van der Zwan, 2002; Ma et al., 2011). Intensified weathering could have promoted clay production in the hinterland, and clay delivery into the Alum Shale sea could increase during wetter periods. Climate change also affect physical weathering associated with freeze-thaw processes during colder winters. It is possible that clay deposition increased during periods with high seasonal contrast (e.g. via weathering) and pyrite formation intensified during periods with low seasonal contrast (e.g. via aeolian dust supply of iron) thus amplifying each other in the observed anti-correlated manner. In any case, this study demonstrates the importance of astronomically forced climatic changes in a putatively ice-free world and opens up new avenues for understanding Earth's climate in the Paleozoic.

5. Conclusion

Our cyclostratigraphic analysis of the Cambrian Alum Shale in the Fågeltofta-2 and Billegrav-2 cores from southern Scandinavia has led to five key discoveries:

1) Milankovitch climate cycles are exquisitely recorded in the late Cambrian Alum Shale Formation. An excellent match between the two investigated drill cores facilitated an astronomical calibration of the early Furongian stratigraphy.
2) These results allowed us to refine the Cambrian timescale and provide durations of 3.4 ± 0.2 Myr for the *Olenus* Superzone (Paibian Stage), 1.9 ± 0.3 Myr for the *Parabolina* Superzone, 0.33 ± 0.18 Myr for the *Leptoplastus* Superzone, 0.51 ± 0.20 Myr for the *Protopeltura* Superzone, and 3.0 ± 0.2 Myr for the SPICE event. The latter is defined here by trends

observed in marine $\delta^{13}C_{org}$.

3) Reconstructed sedimentation rates exhibit similar trends in the two cores and show an inverse relationship to sea level changes.
4) In the mid-Furongian, the Earth's obliquity period, the Earth–Moon distance, and the day length were 31.4 ± 1.2 kyr, $368.9 \pm 2.3 \cdot 10^6$ m, and 21.78 ± 0.29 hours, respectively.
5) The climate cycles are expressed in elements bound to pyrite (S, Fe) and anti-correlated with elements hosted mainly in clay minerals (Al, Ti, K, Si). Plausible drivers for the cyclic sedimentation include airborne dust delivery, eustatic sea level fluctuations, and/or continental weathering.

Acknowledgments

We thank Marie-Louise Siggaard Andersen and Kurt Kjær for assistance and access to the core scanner XRF facility at the GLOBE Institute, and Per Ambus (UCPH) for assistance with carbon isotope analyses at the Department of Geosciences and Natural Resource Management (UCPH). TWD acknowledges funding from the Carlsberg Foundation (CF16–0876) and the Danish Council for Independent Research (DFF - 7014-00295). ATN and NSC acknowledge support from Geocenter Grant 2015–5 and 2017–3. We thank Linda Hinnov for sharing the Taner filter Matlab script at http://mason.gmu.edu/~lhinnov/cyclotools/tanerfilter.m (date: 16.03.2020).

Author contributions:

ALS and TWD designed the study. ATN and NHS provided the drill cores for analyses. ALS, TWD and ZZ collected the data. ALS developed the algorithms used for XRF core scanner data reduction and performed the cyclostratigraphic analysis under supervision of NT and TWD. ALS and TWD wrote the manuscript with input from all authors.

Competing Interests: The authors declare no competing interests.

References

Ahlberg, P., Axheimer, N., Babcock, L.E., Eriksson, M.E., Schmitz, B., Terfelt, F., 2009. Cambrian high-resolution biostratigraphy and carbon isotope chemostratigraphy in Scania, Sweden: first record of the SPICE and DICE excursions in Scandinavia. Lethaia 42, 2–16. https://doi.org/10.1111/j.1502-3931.2008.00127.x

Babcock, L.E., Peng, S.-C., Brett, C.E., Zhu, M.-Y., Ahlberg, P., Bevis, M., Robison, R.A., 2015. Global climate, sea level cycles, and biotic events in the Cambrian Period. Palaeoworld 24, 5–15. https://doi.org/10.1016/j.palwor.2015.03.005

Balslev-Clausen, D., Dahl, T.W., Saad, N., Rosing, M.T., 2013. Precise and accurate δ13C analysis of rock samples using Flash Combustion–Cavity Ring Down Laser Spectroscopy. J. Anal. At. Spectrom. 28, 516. https://doi.org/10.1039/c2ja30240c

Bambach, R.K., Knoll, A.H., Wang, S.C., 2004. Origination, extinction, and mass depletions of marine diversity. Paleobiology 30, 522–542.

Bartlett, B.C., Stevenson, D.J., 2016. Analysis of a Precambrian resonance-stabilized day length. Geophys. Res. Lett. 43, 5716–5724. https://doi.org/10.1002/2016GL068912

Buchardt, B., Nielsen, A.T., 1985. Carbon and oxygen isotope composition of Cambro-Silurian limestone and anthraconite from Bornholm: Evidence for deep burial diagenesis. Bull. Geol. Soc. Den. 33, 415–425.

Buchardt, B., Nielsen, A.T., Schovsbo, N.H., 1997. Alun Skiferen i Skandinavien. Geol. Tidsskr. 3, 1–30.

Da Silva, A.C., Hladil, J., Chadimová, L., Slavík, L., Hilgen, F.J., Bábek, O., Dekkers, M.J., 2016. Refining the Early Devonian time scale using Milankovitch cyclicity in Lochkovian–Pragian sediments (Prague Synform, Czech Republic). Earth Planet. Sci. Lett. 455, 125–139. https://doi.org/10.1016/j.epsl.2016.09.009

Dahl, T.W., Boyle, R.A., Canfield, D.E., Connelly, J.N., Gill, B.C., Lenton, T.M., Bizzarro, M., 2014. Uranium isotopes distinguish two geochemically distinct stages during the later Cambrian SPICE event. Earth Planet. Sci. Lett. 401, 313–326. https://doi.org/10.1016/j.epsl.2014.05.043

Dahl, T.W., Hammarlund, E.U., Anbar, A.D., Bond, D.P.G., Gill, B.C., Gordon, G.W., Knoll, A.H., Nielsen, A.T., Schovsbo, N.H., Canfield, D.E., 2010. Devonian rise in atmospheric oxygen correlated to the radiations of terrestrial plants and large predatory fish. Proc. Natl. Acad. Sci. 107, 17911–17915. https://doi.org/10.1073/pnas.1011287107

Dahl, T.W., Siggaard-Andersen, M.-L., Schovsbo, N.H., Persson, D.O., Husted, S., Hougård, I.W., Dickson, A.J., Kjær, K., Nielsen, A.T., 2019. Brief oxygenation events in locally anoxic oceans during the Cambrian solves the animal breathing paradox. Sci. Rep. 9, 11669. https://doi.org/10.1038/s41598-019-48123-2

Davydov, V.I., Crowley, J.L., Schmitz, M.D., Poletaev, V.I., 2010. High-precision U-Pb zircon age calibration of the global Carboniferous time scale and Milankovitch band cyclicity in the Donets Basin, eastern Ukraine: U-Pb age of the Carboniferous and cyclicity. Geochem. Geophys. Geosystems 11, 1–22. https://doi.org/10.1029/2009GC002736

de Oliveira Carvalho Rodrigues, P., Hinnov, L.A., Franco, D.R., 2019. A new appraisal of depositional cyclicity in the Neoarchean-Paleoproterozoic Dales Gorge Member (Brockman Iron Formation, Hamersley Basin, Australia). Precambrian Res. 328, 27–47. https://doi.org/10.1016/j.precamres.2019.04.007

De Vleeschouwer, D., Boulvain, F., Da Silva, A.-C., Pas, D., Labaye, C., Claeys, P., 2015. The astronomical calibration of the Givetian (Middle Devonian) timescale (Dinant

Synclinorium, Belgium). Geol. Soc. Lond. Spec. Publ. 414, 245–256. https://doi.org/10.1144/SP414.3

De Vleeschouwer, D., Whalen, M.T., (Jed) Day, J.E., Claeys, P., 2012. Cyclostratigraphic calibration of the Frasnian (Late Devonian) time scale (western Alberta, Canada). Geol. Soc. Am. Bull. 124, 928–942. https://doi.org/10.1130/B30547.1

Derby, J.R., Fritz, R.D., Longacre, S.A., Morgan, W.A., Sternbach, C.A., American Association of Petroleum Geologists (Eds.), 2012. The great American carbonate bank: the geology and economic resources of the Cambrian-Ordovician Sauk megasequence of Laurentia, AAPG memoir. American Association of Petroleum Geologists : Shell Corporation, Tulsa, OK.

Ellwood, B.B., El Hassani, A., Tomkin, J.H., Bultynck, P., 2015. A climate-driven model using time-series analysis of magnetic susceptibility (χ) datasets to represent a floating-point high-resolution geological timescale for the Middle Devonian Eifelian stage. Geol. Soc. Lond. Spec. Publ. 414, 209–223. https://doi.org/10.1144/SP414.4

Fang, J., Wu, H., Fang, Q., Shi, M., Zhang, S., Yang, T., Li, H., Cao, L., 2020. Cyclostratigraphy of the global stratotype section and point (GSSP) of the basal Guzhangian Stage of the Cambrian Period. Palaeogeogr. Palaeoclimatol. Palaeoecol. 540, 109530. https://doi.org/10.1016/j.palaeo.2019.109530

Fang, Q., Wu, H., Hinnov, L.A., Jing, X., Wang, X., Yang, T., Li, H., Zhang, S., 2017. Astronomical cycles of Middle Permian Maokou Formation in South China and their implications for sequence stratigraphy and paleoclimate. Palaeogeogr. Palaeoclimatol. Palaeoecol. 474, 130–139. https://doi.org/10.1016/j.palaeo.2016.07.037

Gambacorta, G., Menichetti, E., Trincianti, E., Torricelli, S., 2018. Orbital control on cyclical primary productivity and benthic anoxia: Astronomical tuning of the Telychian Stage (Early Silurian). Palaeogeogr. Palaeoclimatol. Palaeoecol. 495, 152–162. https://doi.org/10.1016/j.palaeo.2018.01.003

Gill, B. C., Lyons, T.W., Young, S.A., Kump, L.R., Knoll, A.H., Saltzman, M.R., 2011. Geochemical evidence for widespread euxinia in the later Cambrian ocean. Nature 469, 80–3. https://doi.org/10.1038/nature09700

Hansen, K., 1945. The Middle and Upper Cambrian sedimentary rocks of Bornholm. Dan. Geol. Unders. 2, 81.

Hearing, T.W., Harvey, T.H.P., Williams, M., Leng, M.J., Lamb, A.L., Wilby, P.R., Gabbott, S.E., Pohl, A., Donnadieu, Y., 2018. An early Cambrian greenhouse climate. Sci. Adv. 4, eaar5690. https://doi.org/10.1126/sciadv.aar5690

Hilgen, F., Lourens, L., Pälike, H., research support team, 2020. Should Unit-Stratotypes and Astrochronozones be formally defined? A dual proposal (including postscriptum). Newsl. Stratigr. 53, 19–39. https://doi.org/10.1127/nos/2019/0514

Hinnov, L.A., 2018. Cyclostratigraphy and Astrochronology in 2018, in: Stratigraphy & Timescales. Elsevier, pp. 1–80. https://doi.org/10.1016/bs.sats.2018.08.004

Hofmann, A., Dirks, P.H.G.M., Jelsma, H.A., 2004. Shallowing-Upward Carbonate Cycles in the Belingwe Greenstone Belt, Zimbabwe: A Record of Archean Sea-Level Oscillations. J. Sediment. Res. 74, 64–81. https://doi.org/10.1306/052903740064

Huang, H., Gao, Y., Jones, M.M., Tao, H., Carroll, A.R., Ibarra, D.E., Wu, H., Wang, C., 2020. Astronomical forcing of Middle Permian terrestrial climate recorded in a large paleolake in northwestern China. Palaeogeogr. Palaeoclimatol. Palaeoecol. 550, 109735. https://doi.org/10.1016/j.palaeo.2020.109735

Kutzbach, J.E., 1997. Response of the African Monsoon to Orbital Forcing and Ocean Feedbacks in the Middle Holocene. Science 278, 440–443. https://doi.org/10.1126/science.278.5337.440

Laskar, J., Robutel, P., Joutel, F., Gastineau, M., Correia, A.C.M., Levrard, B., 2004. A long-term numerical solution for the insolation quantities of the Earth. Astron. Astrophys. 428, 261–285. https://doi.org/10.1051/0004-6361:20041335

Li, M., Hinnov, L., Kump, L., 2019. Acycle: Time-series analysis software for paleoclimate research and education. Comput. Geosci. 127, 12–22. https://doi.org/10.1016/j.cageo.2019.02.011

Lowrie, W., 2007. Fundamentals of geophysics. Cambridge University Press, Cambridge.

Ma, W., Tian, J., Li, Q., Wang, P., 2011. Simulation of long eccentricity (400-kyr) cycle in ocean carbon reservoir during Miocene Climate Optimum: Weathering and nutrient response to orbital change: The 400-kyr cycle of oceanic δ^{13}C. Geophys. Res. Lett. 38, 1–5. https://doi.org/10.1029/2011GL047680

Mann, M.E., Lees, J.M., 1996. Robust estimation of background noise and signal detection in climatic time series. Clim. Change 33, 409–445. https://doi.org/10.1007/BF00142586

Meyers, S.R., 2015. The evaluation of eccentricity-related amplitude modulation and bundling in paleoclimate data: An inverse approach for astrochronologic testing and time scale optimization: Astrochronologic testing and optimization. Paleoceanography 30, 1625–1640. https://doi.org/10.1002/2015PA002850

Nielsen, A.T., Høyberget, M., Ahlberg, P., 2020. The Furongian (upper Cambrian) Alum Shale of Scandinavia: revision of zonation. Lethaia let.12370, 1–24. https://doi.org/10.1111/let.12370

Nielsen, A.T., Schovsbo, N.H., 2015. The regressive Early-Mid Cambrian 'Hawke Bay Event' in Baltoscandia: Epeirogenic uplift in concert with eustasy. Earth-Sci. Rev. 151, 288–350. https://doi.org/10.1016/j.earscirev.2015.09.012

Nielsen, A.T., Schovsbo, N.H., 2007. Cambrian to basal Ordovician lithostratigraphy in Southern Scandinavia. Bull. Geol. Soc. Den. 53, 47–92.

Nielsen, A.T., Schovsbo, N.H., Klitten, K., Woollhead, D., Rasmussen, C., 2018. Gamma-ray log correlation and stratigraphic architecture of the Cambro-Ordovician Alum Shale Formation on Bornholm, Denmark: Evidence for differential syndepositional isostasy. Bull. Geol. Soc. Den. 66, 237–273.

Ogg, J.G., Ogg, G.M., Gradstein, F.M., 2016. Cambrian, in: A Concise Geologic Time Scale. Elsevier, pp. 41–55. https://doi.org/10.1016/B978-0-444-59467-9.00005-4

Osleger, D., Read, J.F., 1991. Relation of Eustasy to Stacking Patterns of Meter-Scale Carbonate Cycles, Late Cambrian, U.S.A. J. Sediment. Petrol. 61, 1225–1252.

Pas, D., Hinnov, L., Day, J.E. (Jed), Kodama, K., Sinnesael, M., Liu, W., 2018. Cyclostratigraphic calibration of the Famennian stage (Late Devonian, Illinois Basin, USA). Earth Planet. Sci. Lett. 488, 102–114. https://doi.org/10.1016/j.epsl.2018.02.010

Peng, S., Babcock, L.E., Cooper, R.A., 2012. The Cambrian Period, in: The Geologic Time Scale. Elsevier, pp. 437–488. https://doi.org/10.1016/B978-0-444-59425-9.00019-6

Raiswell, R., Canfield, D.E., 2012. The Iron Biogeochemical Cycle Past and Present. Geochem. Perspect. 1, 1–220. https://doi.org/10.7185/geochempersp.1.1

Saltzman, M.R., Ripperdan, R.L., Brasier, M.D., Lohmann, K.C., Robison, R.A., Chang, W.T., Peng, S., Ergaliev, E.K., Runnegar, B., 2000. A global carbon isotope excursion (SPICE) during the Late Cambrian: relation to trilobite extinctions, organic-matter burial and sea level. Palaeogeogr. Palaeoclimatol. Palaeoecol. 162, 211–223. https://doi.org/10.1016/S0031-0182(00)00128-0

Saltzman, M.R., Young, S.A., Kump, L.R., Gill, B.C., Lyons, T.W., Runnegar, B., 2011. Pulse of atmospheric oxygen during the late Cambrian. Proc. Natl. Acad. Sci. 108, 3876–3881. https://doi.org/10.1073/pnas.1011836108

Scotese, C.R., 2014. Scotese, C.R., 2014. Atlas of Neogene Paleogeographic Maps (Mollweide Projection), Maps 1-7, Volume 1, The Cenozoic, PALEOMAP Atlas for ArcGIS, PALEOMAP Project, Evanston, IL. https://doi.org/10.13140/2.1.4151.3922

Schwarz, G., 1978. Estimating the Dimension of a Model. Ann. Stat. 6, 461–464. https://doi.org/10.1214/aos/1176344136

Taner, M.T., Koehler, F., Sheriff, R.E., 1979. Complex seismic trace analysis. GEOPHYSICS 44, 1041–1063. https://doi.org/10.1190/1.1440994

Thomson, D.J., 1982. Spectrum estimation and harmonic analysis. Proc. IEEE 70, 1055–1096. https://doi.org/10.1109/PROC.1982.12433

Van der Zwan, C.J., 2002. The impact of Milankovitch-scale climatic forcing on sediment supply. Sediment. Geol. 147, 271–294. https://doi.org/10.1016/S0037-0738(01)00130-0

Vaughan, S., Bailey, R.J., Smith, D.G., 2011. Detecting cycles in stratigraphic data: Spectral analysis in the presence of red noise. Paleoceanography 26, 1–15. https://doi.org/10.1029/2011PA002195

Walker, J.C.G., Zahnle, K.J., 1986. Lunar nodal tide and distance to the Moon during the Precambrian. Nature 320, 600–602. https://doi.org/10.1038/320600a0

Waltham, D., 2015. Milankovitch Period Uncertainties and Their Impact On Cyclostratigraphy. J. Sediment. Res. 85, 990–998. https://doi.org/10.2110/jsr.2015.66

Weidner, T., Nielsen, A.T., 2014. Agraulos longicephalus and Proampyx? depressus (Trilobita) from the Middle Cambrian of Bornholm, Denmark. Bull. Geol. Soc. Den. 63, 1–11.

Wotte, T., Skovsted, C.B., Whitehouse, M.J., Kouchinsky, A., 2019. Isotopic evidence for temperate oceans during the Cambrian Explosion. Sci. Rep. 9, 6330. https://doi.org/10.1038/s41598-019-42719-4

Wu, H., Zhang, S., Hinnov, L.A., Jiang, G., Feng, Q., Li, H., Yang, T., 2013. Time-calibrated Milankovitch cycles for the late Permian. Nat. Commun. 4, 2452. https://doi.org/10.1038/ncomms3452

Zahnle, K., Walker, J.C.G., 1987. A constant daylength during the precambrian era? Precambrian Res. 37, 95–105. https://doi.org/10.1016/0301-9268(87)90073-8

Zhang, S., Wang, X., Hammarlund, E.U., Wang, H., Costa, M.M., Bjerrum, C.J., Connelly, J.N., Zhang, B., Bian, L., Canfield, D.E., 2015. Orbital forcing of climate 1.4 billion years ago. Proc. Natl. Acad. Sci. 112, E1406–E1413. https://doi.org/10.1073/pnas.1502239112

Zhong, Y., Wu, H., Zhang, Y., Zhang, S., Yang, T., Li, H., Cao, L., 2018. Astronomical calibration of the Middle Ordovician of the Yangtze Block, South China. Palaeogeogr. Palaeoclimatol. Palaeoecol. 505, 86–99. https://doi.org/10.1016/j.palaeo.2018.05.030

Figure captions

Figure 1. Geological setting of the studied cores. A) Paleogeographic Map of the Furongian Earth (Scotese, 2014) showing the location of Baltica where the Alum Shale was deposited at the time. B) Isopach map of the Furongian Alum Shale in southern Scandinavia (thickness in meters). Modified from Nielsen et al. (2020). C) Typical appearance of the Alum Shale drill core, which is black and monotonous with no visual signs of cycles. Photograph taken by the XRF core scanner of a 0.55 m interval of the Fågeltofta-2 core (88.07 – 88.62 m, *Agnostus pisiformis* Zone). White intervals represent vax used to glue broken core pieces together prior to scanning (see supplementary material for details). D) Scandinavian trilobite zonation of the stratigraphic intervals investigated in the Fågeltofta-2 and Billegrav-2 cores. Abbreviations: M. – Miaolingian, G. –Guzhangian. Based on Nielsen et al. (2020).

Figure 2. MTM power spectra for A) Fågeltofta-2 and B) Billegrav-2 cores with the corresponding wavelet spectrograms shown in C and D. The four taper MTM power spectra of the detrended sulfur content is shown with bending power low noise model and confidence levels. The "bumb" wavelet is sensitive to high frequency variations in the signal (<8 kyr), so we have used a 100-point smoothing to highlight the observed cycles in the wavelet spectrograms. Abbreviations: Ap= *Agnostus pisiformis* Zone*,* Ol = *Olenus* Superzone, Pa =*Parabolina* Superzone, Le = *Leptoplastus* Superzone, Pr = *Protopeltura* Superzone, Pe = *Peltura* Superzone.

Figure 3. Stratigraphic correlation of the detrended and smoothed sulfur content (blue curves), the 405 kyr filtered outputs (red curves), and molybdenum profile (green curve) between the Fågeltofta-2 and Billegrav-2 drill cores. Each 405 kyr eccentricity cycles are named according to the zone/superzone (Ap= *Agnostus pisiformis*, Ol = *Olenus*, Pa = *Parabolina*, Le = *Leptoplastus*, Pr

= *Protopeltura*, Pe = *Peltura*) and numbered from the youngest to the oldest according to conventional astrochronology. The Mo and detrended S curves are smoothed with a window of 300 data points (corresponding to 60 mm) in both cores to visually emphasize the cycles and the longer-term stratigraphic trends in the Mo curve. The filtered outputs of the detrended S contents have Taner filter settings with centers and cut-offs at 1.4 m (1.0 –2.1 m) and 0.66 m (0.5–1.0 m) for Fågeltofta-2 and Billegrav-2, respectively. Grey area in Pa-2 in Billegrav-2 marks an inferred hiatus and the question mark indicates the corresponding unknown correlation of Pa-2 between the two cores. The Guzhangian-Paibian boundary is defined at the first appearance datum (FAD) of *Glyptagnostus reticulatus* in a thick slope section in South China (Peng et al. 2012). This fossil appears a few cm above the FAD of *Olenus gibbosus*, which is used to define the base of the Paibian in Scandinavia. Hence, the Ap/Ol boundary is essentially equal to the base of the Furongian.

Figure 4. Four taper MTM power spectra of the detrended sulfur time-series in frequency domain (series calibrated to the 405-kyr eccentricity rhythm as shown in Fig. 3). Black vertical lines represent the expected theoretical Milankovitch periods for the Earth at 497 Ma and the grey areas represent uncertainties for these periods (17.0 ± 1.1, 16.9 ± 1.1, 19.6 ± 1.4, 20.6 ± 1.6, 32.6 ± 4.0, 94.9 ± 1.4, 98.9 ± 1.5, 123.9 ± 2.6, 130.8 ± 2.9 and 405.6 ± 2.4 kyr based on Waltham, 2015). Bending power laws are used as noise models in panel A, B and D, whereas ARMA(4,21) is used in panel C. The ARMA(i,j) model parameters were determined using the Schwarz Information Criteria (Schwarz, 1978) among 250 models where i = 1, 2, … , 10 and j = 1, 2, …, 25. CL = confidence levels.

Figure 5. Amplitude of precession (red) and obliquity (black) cycles across the *A. Pisiformis-Olenus* boundary showing eccentricity amplitude modulations (AM) of the precession band in the Fågeltofta-2 core. The age axis is anchored at the Miaolingian/Furongian boundary set to 497.00 Ma (Peng et al., 2012). The black curve corresponds to the amplitude envelope of the precession, and the numbers above the envelope indicate the calculated durations of each AM cycles in kyr. Note the sudden switch from high amplitude 32 kyr obliquity forcing in the upper *Agnostus pisiformis* Zone to high amplitude 18 kyr precession forcing in the *Olenus* Superzone.

Figure 6. Summary of results from the two cores. The indicated ages are anchored in the ~497 Ma age estimate for the Miaolingian–Furongian boundary (Peng et al., 2012). A) The calculated sedimentation rates are based on the 405 kyr eccentricity cycles (black dotted lines on Fig. 3). The red and blue curves represent 10^{th} and 18^{th} degree polynomial fits to the sedimentation rates in the Fågeltofta-2 and Billegrav-2 cores, respectively. Sedimentation rates are also calculated using the eCOCO algorithm (grey circles) with default settings and theoretical astronomical periods at 1,925 Ma (Berger89 solution) with a sliding stratigraphic window size of 3 m and 4 m for Få-2 and Bi-2, respectively. The algorithm utilizes a Monte Carlo approach to obtain sedimentation rates from a possible range of values chosen to 0.2–0.6 and 0.01–0.3 cm/kyr for the Få-2 and Bi-2 core, respectively. B) A best-estimated sea level curve obtained by smoothing the curve of Nielsen et al. (2020) and reinterpreting some of the 3^{rd} and 4^{th} order oscillations. C) Filtered outputs of the sulfur signals using a Taner filter centred at 405 kyr with cut-offs at 360 and 463 kyr. D) Molybdenum content smoothed with a window of 500 data points to emphasize the longer-term stratigraphic trends. E) $\delta^{13}C$ profiles of bulk organic carbon. Abbreviations as in Fig. 3.

Figure 7. The ~32-kyr obliquity (black) and ~100-kyr eccentricity (red) cycles expressed in the upper *Parabolina* Superzone of Fågeltofta-2 spanning the four 405-kyr eccentricity cycles Pa-1, Pa-2, Pa-3 and Pa-4. Four taper MTM power spectra are shown for A) the detrended sulfur signal, and for the same signal normalized to 405-kyr eccentricity cycles in B). Black vertical lines and grey areas show the predicted Milankovitch periods and their uncertainties as in Fig. 4. The normalized curve is derived by subtracting the orange curve from the blue curve in panel C. Both the 32 kyr and 100 kyr periods are significant at the $P < 0.01$ level for the normalized curve. The cycles are visualized in panel C with the calculated durations of each of the cycles in kyr shown on the graph. CL = Confidence Level.

Figure 8. Evolution of the Earth–Moon distance over the past 1500 Myr. Present rate of tidal dissipation (blue curve) and 'Ocean model' (purple curve) are model predictions from Waltham (2015) (see equations in the SI). Here, the model parameters are chosen so that the Earth–Moon distance was zero at 4.5 Ga and the characteristic timescale for changes in resonance strength is 1 Gyr (Waltham, 2015). Observational data from the Mansfield, Elatina, and Big Cottonwood Canyon Formations are derived from tidal rhythmites (tidal bundles related to neap–spring cycles), whereas data from the Walvis Ridge, Lucaogou, Xiamaling and Alum Shale Formations are based on Milankovitch cycles. The uncertainty of the unit ages is smaller than the symbol size except for the Big Cottonwood Canyon Formation. Tabulated data and references are summarized in the supplementary material. See Fig. S9 for the same data and models plotted over the entire history of the Earth.

Figure 1

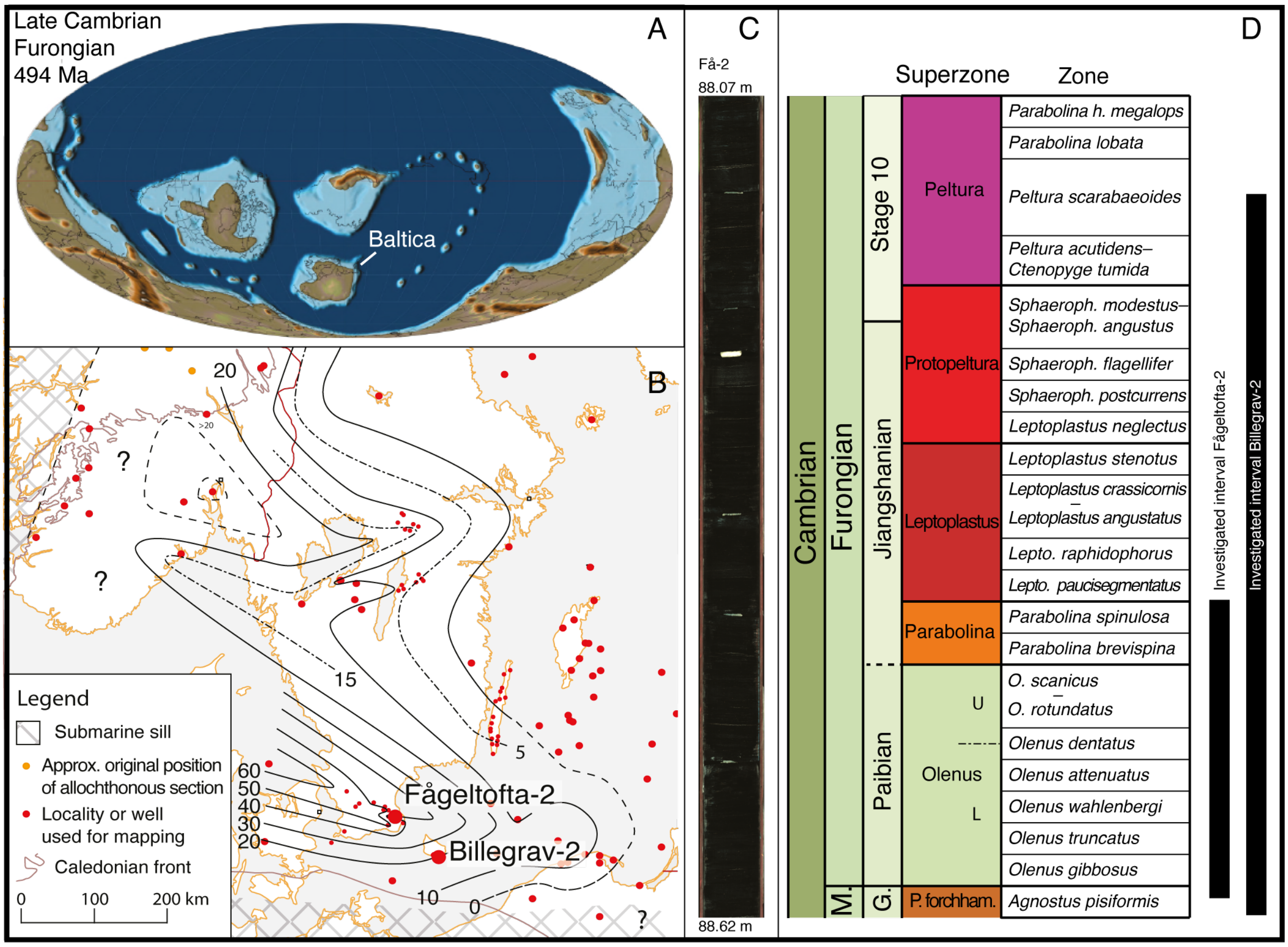

Late Cambrian
Furongian
494 Ma
A
Baltica
B
C
D
Få-2
88.07 m
88.62 m
Legend
Submarine sill
Approx. original position of allochthonous section
Locality or well used for mapping
Caledonian front
0
100
200 km
Fågeltofta-2
Billegrav-2
Superzone
Zone
Cambrian
Furongian
Stage 10
Jiangshanian
Paibian
M.
G.
Peltura
Protopeltura
Leptoplastus
Parabolina
Olenus
U
L
P. forchham.
Parabolina h. megalops
Parabolina lobata
Peltura scarabaeoides
Peltura acutidens–Ctenopyge tumida
Sphaeroph. modestus–Sphaeroph. angustus
Sphaeroph. flagellifer
Sphaeroph. postcurrens
Leptoplastus neglectus
Leptoplastus stenotus
Leptoplastus crassicornis
Leptoplastus angustatus
Lepto. raphidophorus
Lepto. paucisegmentatus
Parabolina spinulosa
Parabolina brevispina
O. scanicus
O. rotundatus
Olenus dentatus
Olenus attenuatus
Olenus wahlenbergi
Olenus truncatus
Olenus gibbosus
Agnostus pisiformis
Investigated interval Fågeltofta-2
Investigated interval Billegrav-2

Figure 2

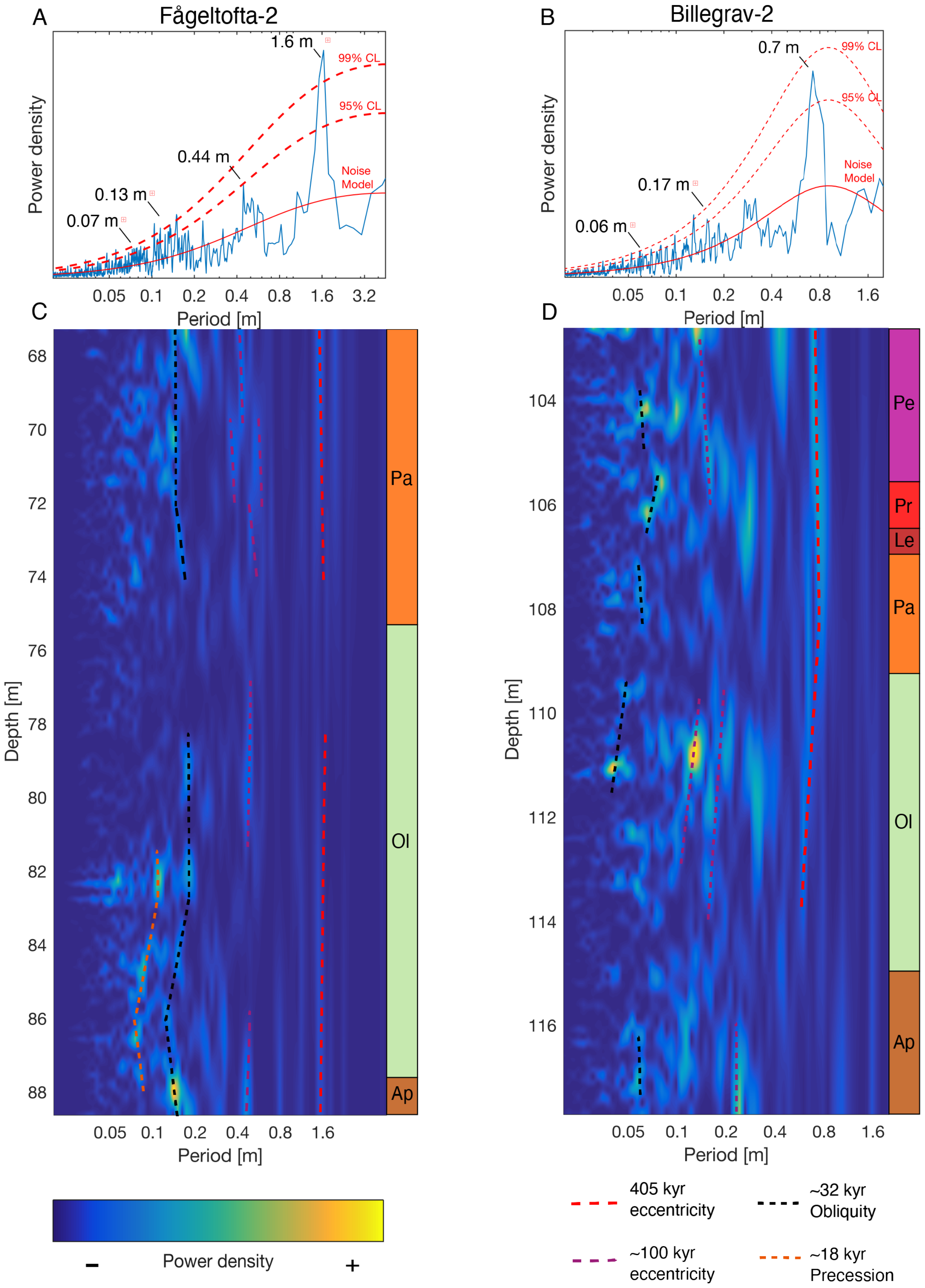

A
Fågeltofta-2
B
Billegrav-2
Power density
1.6 m
99% CL
95% CL
Noise Model
0.44 m
0.13 m
0.07 m
0.7 m
0.17 m
0.06 m
0.05 0.1 0.2 0.4 0.8 1.6 3.2
Period [m]
C
D
Depth [m]
68 70 72 74 76 78 80 82 84 86 88
104 106 108 110 112 114 116
Pa
Ol
Ap
Pe
Pr
Le
Power density
405 kyr eccentricity
~32 kyr Obliquity
~100 kyr eccentricity
~18 kyr Precession

Figure 3

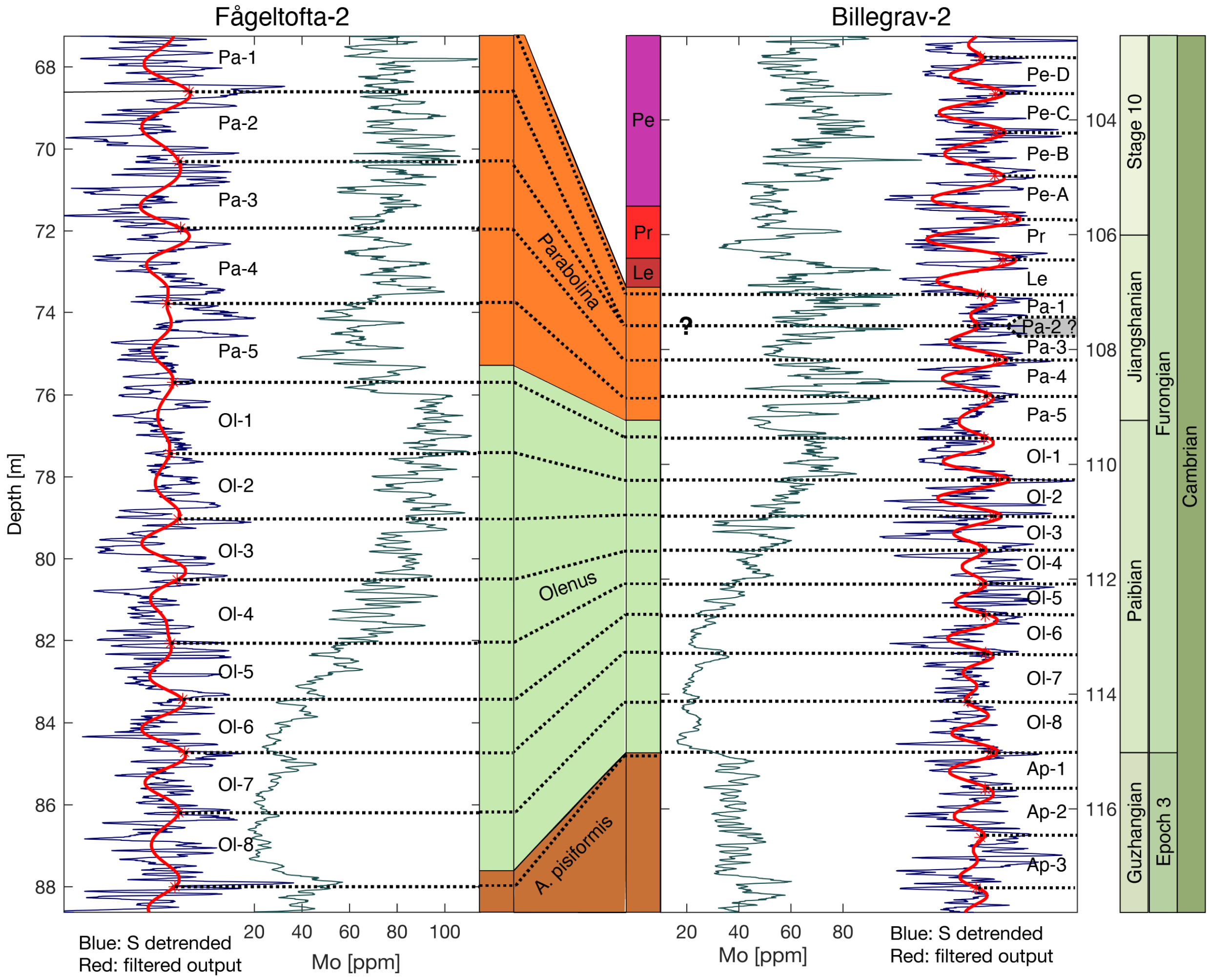

Fågeltofta-2
Billegrav-2
Depth [m]
68
70
72
74
76
78
80
82
84
86
88
Pa-1
Pa-2
Pa-3
Pa-4
Pa-5
Ol-1
Ol-2
Ol-3
Ol-4
Ol-5
Ol-6
Ol-7
Ol-8
20 40 60 80 100
Mo [ppm]
Blue: S detrended
Red: filtered output
Parabolina
Olenus
A. pisiformis
Pe
Pr
Le
?
20 40 60 80
Mo [ppm]
Blue: S detrended
Red: filtered output
Pe-D
Pe-C
Pe-B
Pe-A
Pr
Le
Pa-1
Pa-2 ?
Pa-3
Pa-4
Pa-5
Ol-1
Ol-2
Ol-3
Ol-4
Ol-5
Ol-6
Ol-7
Ol-8
Ap-1
Ap-2
Ap-3
104
106
108
110
112
114
116
Stage 10
Jiangshanian
Paibian
Guzhangian
Furongian
Epoch 3
Cambrian

Figure 4

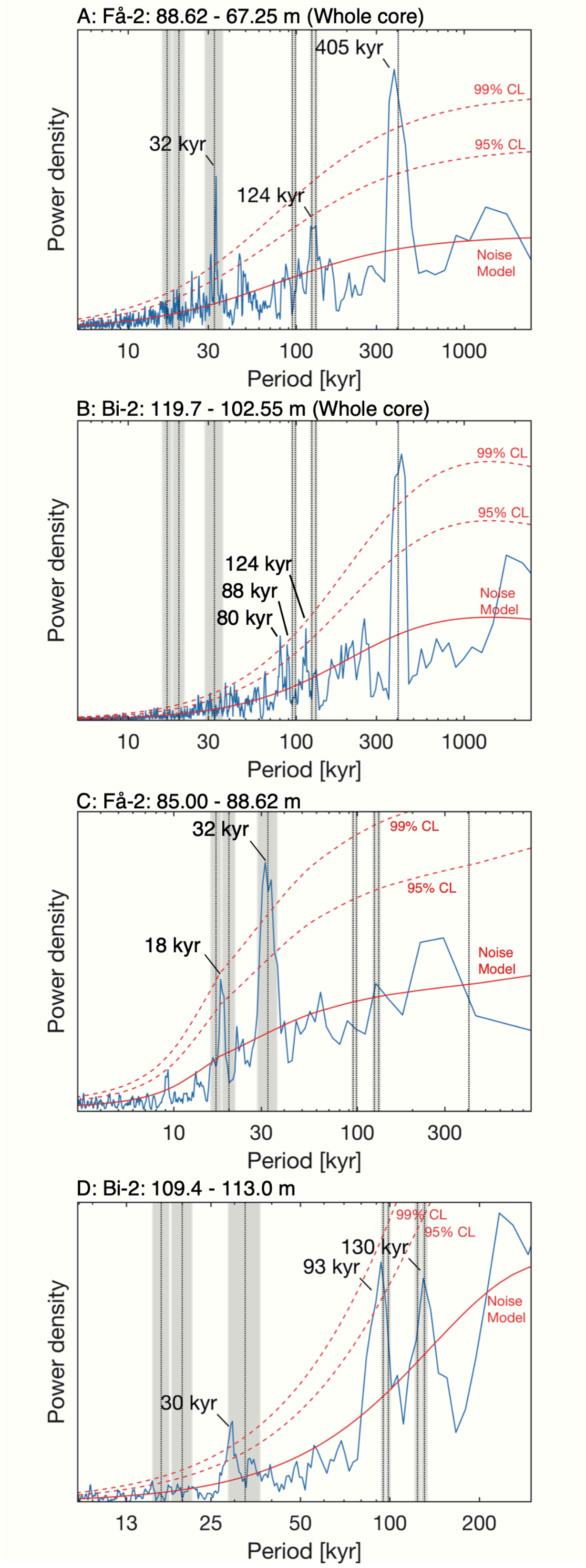

A: Få-2: 88.62 - 67.25 m (Whole core)
405 kyr
99% CL
95% CL
32 kyr
124 kyr
Noise Model
Power density
10
30
100
300
1000
Period [kyr]
B: Bi-2: 119.7 - 102.55 m (Whole core)
99% CL
95% CL
124 kyr
88 kyr
80 kyr
Noise Model
Power density
10
30
100
300
1000
Period [kyr]
C: Få-2: 85.00 - 88.62 m
32 kyr
99% CL
95% CL
18 kyr
Noise Model
Power density
10
30
100
300
Period [kyr]
D: Bi-2: 109.4 - 113.0 m
99% CL
95% CL
130 kyr
93 kyr
Noise Model
30 kyr
Power density
13
25
50
100
200
Period [kyr]

Figure 5

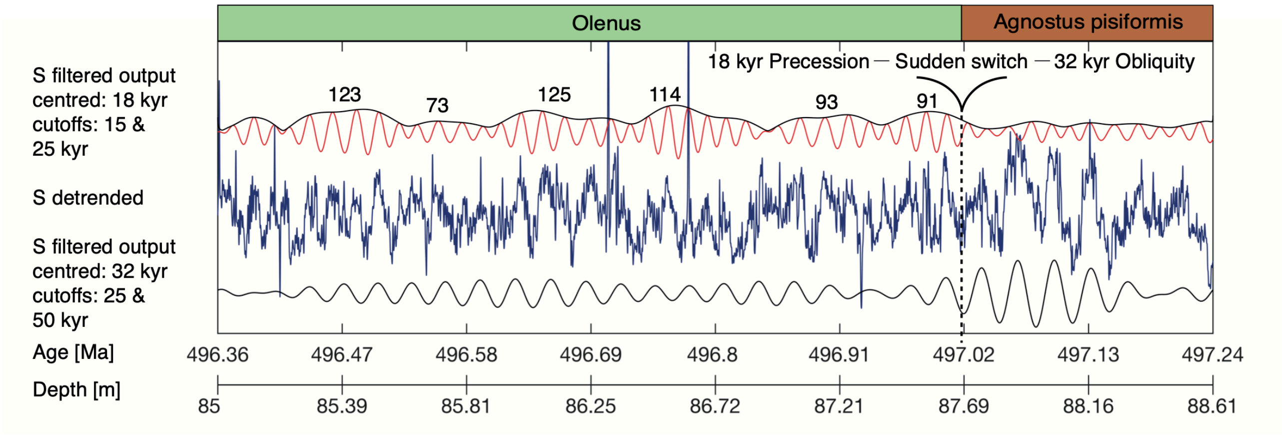
Olenus
Agnostus pisiformis
18 kyr Precession — Sudden switch — 32 kyr Obliquity
123
73
125
114
93
91
S filtered output centred: 18 kyr cutoffs: 15 & 25 kyr
S detrended
S filtered output centred: 32 kyr cutoffs: 25 & 50 kyr
Age [Ma]
496.36
496.47
496.58
496.69
496.8
496.91
497.02
497.13
497.24
Depth [m]
85
85.39
85.81
86.25
86.72
87.21
87.69
88.16
88.61

Figure 6

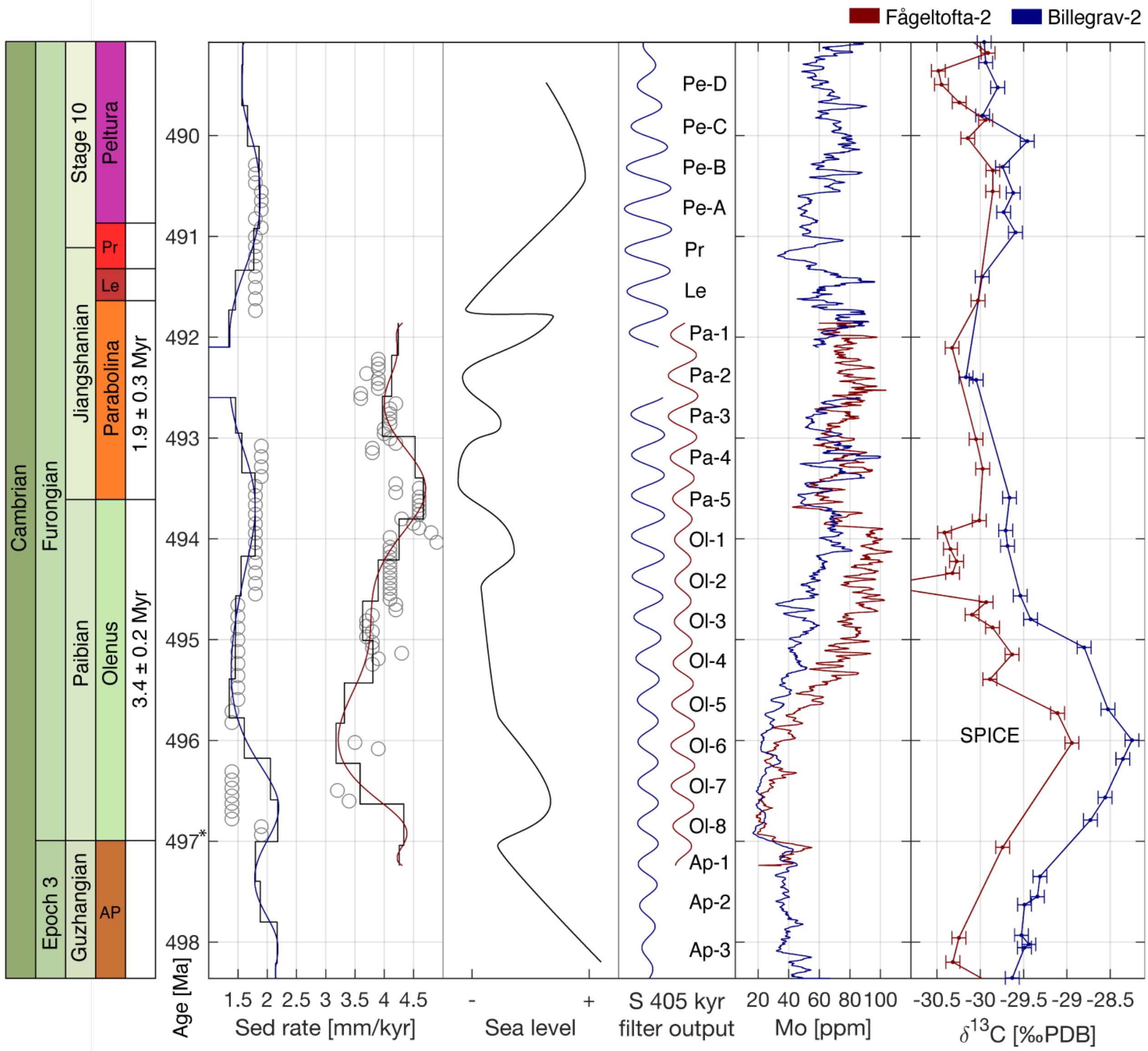

Fågeltofta-2
Billegrav-2
Cambrian
Furongian
Epoch 3
Stage 10
Jiangshanian
Paibian
Guzhangian
Peltura
Pr
Le
Parabolina
Olenus
AP
1.9 ± 0.3 Myr
3.4 ± 0.2 Myr
490
491
492
493
494
495
496
497*
498
Age [Ma]
1.5 2 2.5 3 3.5 4 4.5
Sed rate [mm/kyr]
- +
Sea level
Pe-D
Pe-C
Pe-B
Pe-A
Pr
Le
Pa-1
Pa-2
Pa-3
Pa-4
Pa-5
Ol-1
Ol-2
Ol-3
Ol-4
Ol-5
Ol-6
Ol-7
Ol-8
Ap-1
Ap-2
Ap-3
S 405 kyr filter output
20 40 60 80 100
Mo [ppm]
SPICE
-30.5 -30 -29.5 -29 -28.5
δ13C [‰PDB]

Figure 7

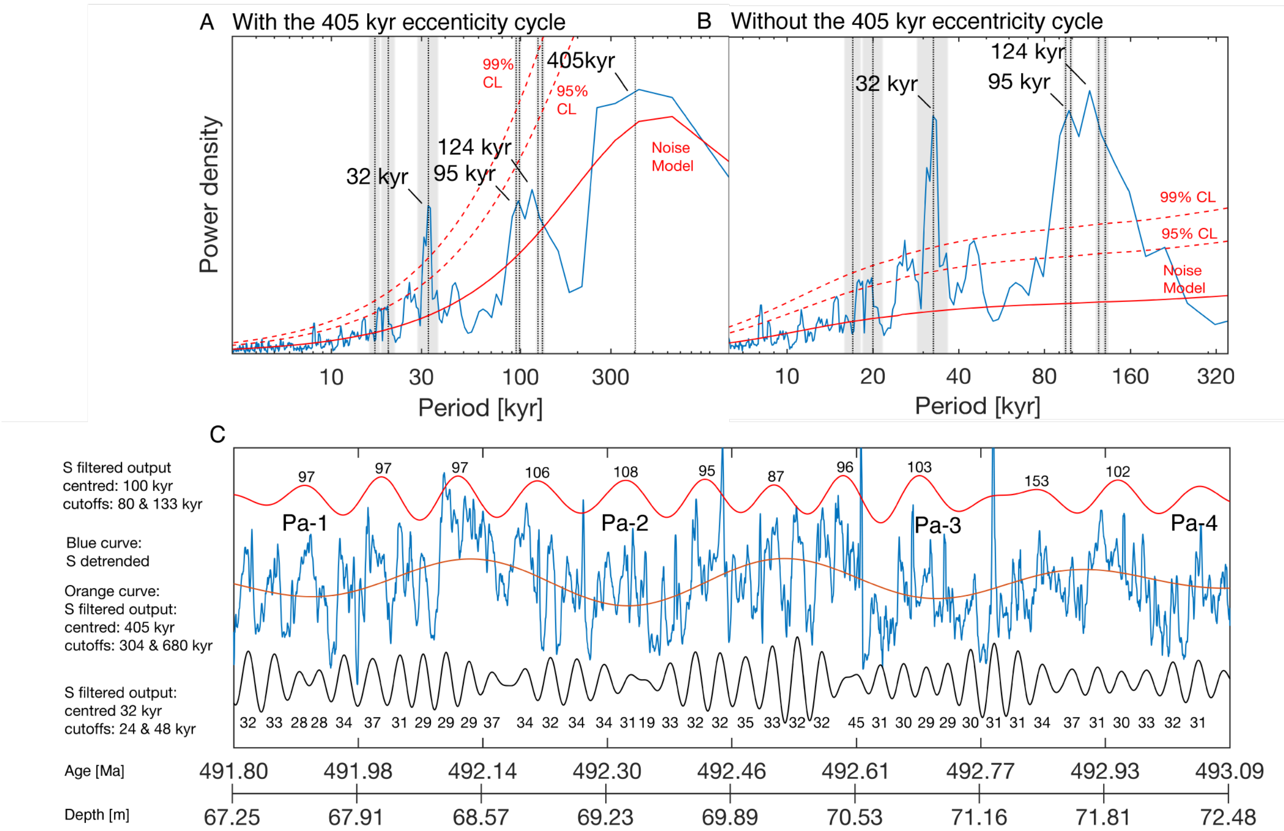

A With the 405 kyr eccenticity cycle
B Without the 405 kyr eccentricity cycle
Power density
Period [kyr]
405kyr
124 kyr
95 kyr
32 kyr
99% CL
95% CL
Noise Model
C
S filtered output
centred: 100 kyr
cutoffs: 80 & 133 kyr
Blue curve:
S detrended
Orange curve:
S filtered output:
centred: 405 kyr
cutoffs: 304 & 680 kyr
S filtered output:
centred 32 kyr
cutoffs: 24 & 48 kyr
Pa-1
Pa-2
Pa-3
Pa-4
Age [Ma]
491.80 491.98 492.14 492.30 492.46 492.61 492.77 492.93 493.09
Depth [m]
67.25 67.91 68.57 69.23 69.89 70.53 71.16 71.81 72.48

Figure 8

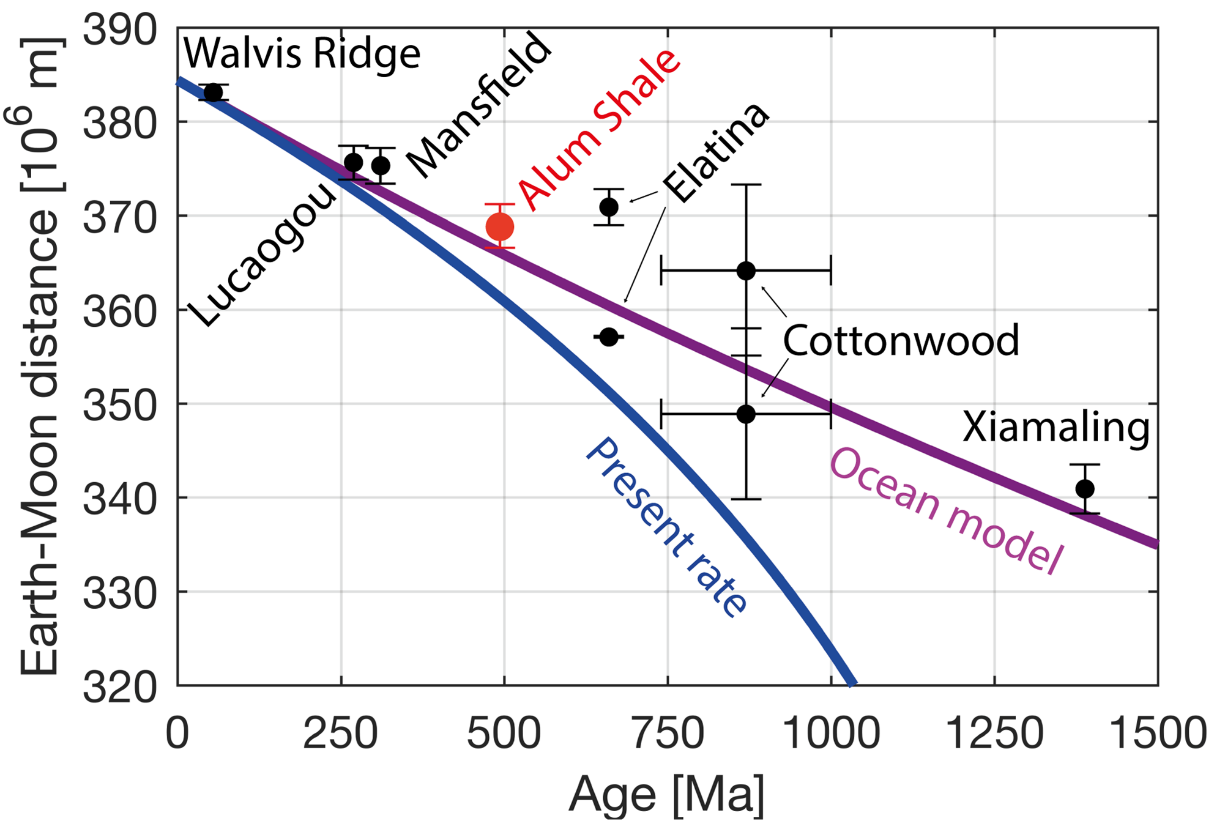

Walvis Ridge
Mansfield
Lucaogou
Alum Shale
Elatina
Cottonwood
Xiamaling
Ocean model
Present rate
390
380
370
360
350
340
330
320
Earth-Moon distance [10^6 m]
0
250
500
750
1000
1250
1500
Age [Ma]